

Validation of 3D reconstructions of a mimicked femoral artery with an ultrasound imaging robotic system

Marie-Ange Janvier^{a)}

Laboratory of Biorheology and Medical Ultrasonics, Research Centre of the Centre Hospitalier de l'Université de Montréal (CRCHUM), Montréal, Québec H2L 2W5, Canada and Institute of Biomedical Engineering, Université de Montréal, Montréal, Québec H3T 1J4, Canada

Gilles Soulez

Institute of Biomedical Engineering, Université de Montréal, Montréal, Québec, H3T 1J4 Canada; Department of Radiology, Centre Hospitalier de l'Université de Montréal (CHUM), Montréal, Québec H2L 4M1, Canada; and Department of Radiology, Radio-Oncology and Nuclear Medicine, Université de Montréal, Montréal, Québec H3T 1J4, Canada

Louise Allard

Laboratory of Biorheology and Medical Ultrasonics, Research Centre of the Centre Hospitalier de l'Université de Montréal (CRCHUM), Montréal, Québec H2L 2W5, Canada

Guy Cloutier^{b)}

Laboratory of Biorheology and Medical Ultrasonics, Research Centre of the Centre Hospitalier de l'Université de Montréal (CRCHUM), Montréal, Québec H2L 2W5, Canada; Institute of Biomedical Engineering, Université de Montréal, Montréal, Québec H3T 1J4, Canada; and Department of Radiology, Radio-Oncology and Nuclear Medicine, Université de Montréal, Montréal, Québec H3T 1J4, Canada

(Received 18 December 2009; revised 26 March 2010; accepted for publication 17 May 2010; published 30 June 2010)

Purpose: The degree of stenosis is the most important criterion to assess peripheral arterial disease manifested by atherosclerosis mainly in lower limb arteries. Ultrasound (U.S.) imaging offers low-cost, safe, and convenient options to evaluate this disease, but most U.S. freehand approaches cannot optimally locate stenoses and map lower limb arterial geometries. A 3D-U.S. imaging robotic system that can control and standardize image acquisition by scanning typically encountered diseased arterial lower limb segments is presented and validated with phantoms.

Methods: A Z-phantom calibration procedure was used to characterize spatial transformation of the U.S. probe image plane for different clinical image acquisition settings. Moreover, the accuracy of the calibration transform to reconstruct a lower-limb-mimicking vessel geometry was evaluated with a vascular phantom.

Results: A 3D calibration precision of 0.47 ± 0.27 mm was achieved. Reconstruction errors were less than 1.74 ± 0.08 mm in all 3D vessel representations and the cross-sectional areas of each image section were close to those of gold standard phantom measures. The best reconstruction accuracy (smallest error) was 0.40 ± 0.03 mm.

Conclusion: Altogether, these results demonstrate the potential of the robotic scanner to adequately represent lower limb vessels for the clinical evaluation of stenoses. © 2010 American Association of Physicists in Medicine. [DOI: [10.1118/1.3447721](https://doi.org/10.1118/1.3447721)]

Key words: 3D-ultrasound imaging system, cardiovascular imaging, robotics, ultrasound probe calibration, 3D-ultrasound reconstruction, precision and accuracy evaluations, calibration phantom, lower limb arterial disease, computer-assisted image processing

I. INTRODUCTION

Atherosclerosis is the principal cause of peripheral arterial disease that leads to the progressive narrowing of lower limb arteries.¹⁻³ The 3D location of lesions and the degree of stenosis are the most common criteria for assessing the severity of PAD. Moreover, a map of the entire lower limb vessel is required to prepare an appropriate intervention (e.g., the diameter and length of an angioplasty balloon and stent).^{4,5} In fact, most medical centers perform digital subtraction angiography, computed tomography angiography, or magnetic resonance angiography for the complete representation of lower limb arteries.^{6,7} Although these technologies

yield good to excellent image resolution and even some 3D rendering, they are either too costly, invasive, or ionizing.

Different ultrasound (U.S.) imaging techniques, namely, pulsed-wave Doppler, color Doppler flow imaging, power Doppler angiography, and B-mode imaging, are currently able to detect arterial lesions in lower limbs safely, noninvasively, and at low cost.⁸⁻¹¹ However, it is not easy, with these modalities, to visualize the entire lower limb vascular tree with accuracy within an acceptable time frame. Moreover, the evaluation of atherosclerotic disease with conventional 2D B-mode U.S. is highly operator-dependent.¹²

3D-U.S. imaging can precisely define the degree of stenosis and map its location along the lower limb vascular tree.

Already, many 3D-U.S. systems have been successfully developed and validated in various clinical applications, notably, obstetrics, cardiology, and vascular imaging, to increase diagnostic confidence.¹³ Most of them rely on a freehand U.S. probe-tracking method that produces uneven geometric sampling, adding uncertainty to the reconstruction. Moreover, popular freehand tracking devices (optic and electromagnetic) have operating restrictions: Scanning of small distances, the necessity of a constant line of sight, and avoiding metallic interference.^{14–18}

Robotic systems represent a promising alternative for lower limb stenosis quantification and location¹⁹ because they can simultaneously control and standardize 3D-U.S. acquisition without the limitations of 3D freehand devices. Some medical 3D-U.S. prototype robots have been developed but are exclusively deployed in research^{20–23} because they focus mainly on architectural control and safety designs so that their potential clinical performance has not been evaluated. We proposed a medical robot²⁴ for 3D-U.S. scanning of lower limb vessels. The principal features of this system are its teaching mode that enables the learning of “freehand” scanning accommodated to patients’ legs and its replay mode that reproduces the manually taught path. Clinicians would acquire with this system 2D cross-sectional U.S. images at a controlled speed with x , y , and z registration of coordinates and constant contact pressure for 3D reconstruction. Based on our previous report with this system,²⁴ a high positioning accuracy of the robot end-effector and repeatability were achieved. In the context of the current study, these first-step results were required to assure robustness of this technology to track the U.S. probe position into the robot 3D referential.

A major challenge in either freehand or robotic 3D-U.S. is the precise localization of the image into the referential positioning system (i.e., calibration transform for rotation, translation, and scaling).^{17,25} This information is particularly important as errors in image transform propagate through subsequent stages of 3D reconstruction in image analysis and scaling.²⁶ These errors thus have a major impact on the quality of the reconstructed geometry that enables precise 3D visualization, planning, and accurate image-guided interventions. 3D-U.S. calibration techniques usually require imaging a phantom of known geometry and physical properties with key features that are easily identifiable. The simplest and most common phantom is the point-target (i.e., crossed wires or spherical ball), except that calibration is very tedious, time-consuming, and susceptible to image artifacts produced by the U.S. beam.^{27–29} A calibration wall phantom allows the fastest registration of U.S. images^{25,26,30} but for calibration to be valid, it needs to be scanned at a proper range with a specific protocol. Moreover, reverberations of the U.S. beam by the wall can also affect calibration quality. The Z-phantom is the most efficient method for fast and precise calibration from a single B-scan.^{31–34} In comparison to other calibration methods, it provides the best performance in terms of 3D point reconstruction accuracy.³¹ To the best of our knowledge, no 3D-U.S. studies have validated the effect of calibration transforms on 3D-reconstructed vascular mod-

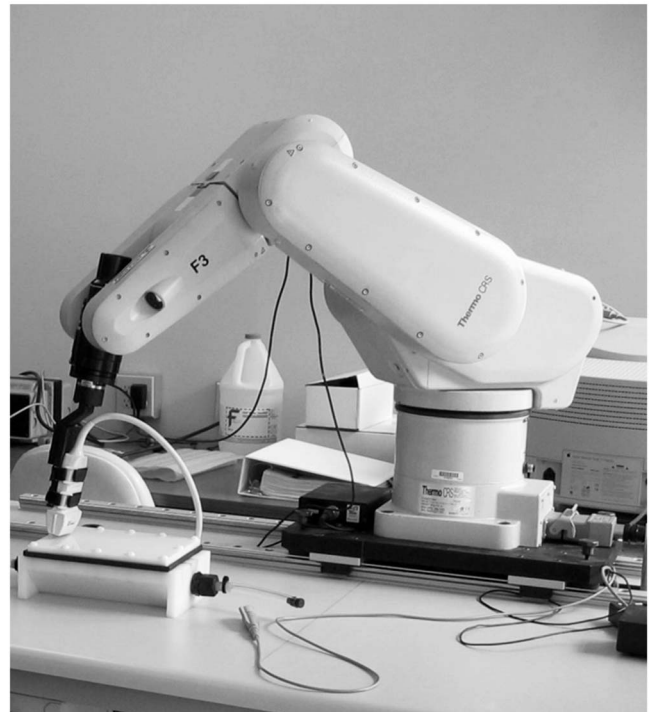


FIG. 1. Overview of the prototype medical robotic 3D-U.S. imaging system (Ref. 24). The robotic arm is moved by a user interface software on the workstation. 2D-U.S. images are tagged with U.S. probe positions acquired from the robotic arm. In this example, a vascular phantom is scanned.

els. The objectives of this study were to adapt a Z calibration procedure for the 3D-U.S. imaging robot and to evaluate its performance in terms of precision and reconstruction accuracy on a 3D vascular geometry with double stenoses.

II. MATERIALS AND METHODS

II.A. Prototype medical robotic 3D-U.S. imaging system

The robotic system illustrated in Fig. 1 includes a computer workstation, the robotic arm (F3 articulated robot, CRS Robotics Corporation, Burlington, Ontario, Canada), and an U.S. echograph. This 3D acquisition scanner, described in detail elsewhere,²⁴ can capture U.S. images at uniform spacing during probe displacement. In the current study, a Vivid-5 echograph system (General Electric, Milwaukee, WI) equipped with a FLA 10 MHz linear array probe was employed. U.S. images were digitized in 480×640 pixel format.

II.B. Calibration procedure

II.B.1. Calibration phantom, experimental setup, data acquisition, and processing

A precise calibration procedure based on a Z-phantom was developed for the 3D-U.S. robotic system (i.e., to identify features that best relate the U.S. image plane location to the phantom space within the robot referential). The design (Fig. 2) consists of a base platform, a container, and the Z-phantom. The square platform incorporates four holes to

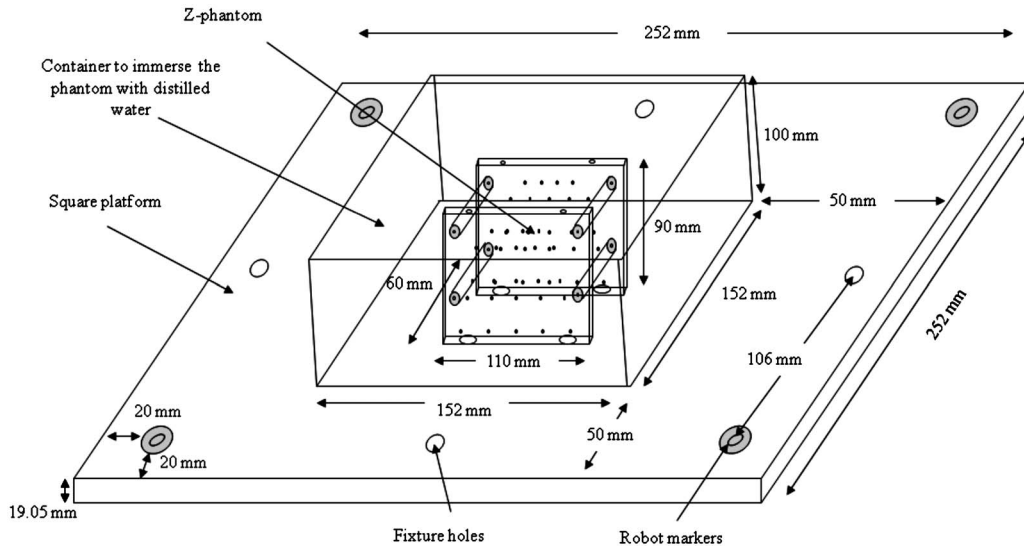


FIG. 2. A complete view of the calibration phantom. It consists of a square platform, a container, and a Z-phantom.

fix the phantom to a table in the robot workspace. This platform also contains four hemispherical steel holes, each 8.38 mm in diameter and 4.19 mm in depth, which serve as markers to localize the phantom in the robot referential. The Z-phantom, inspired by previous works,^{31–34} was immersed in distilled water at room temperature within the container. It consists of two parallel Plexiglas plates (110 mm wide \times 90 mm high \times 9.53 mm thick) positioned 60 mm apart and maintained by four spacers made of high-density polyethylene. Each plate encloses 24 drilled holes of 0.46 mm diameter aligned in five different rows with 10–20 mm gaps. A surgical blue monofilament polypropylene suture wire of 0.07–0.099 mm diameter (8726 Prolene 6–0, Ethicon Inc., Piscataway, NJ) was interwoven through the holes to construct 19 Z-shaped patterns (i.e., Z-fiducials), as depicted in Fig. 3.

The U.S. probe was fixed with a holder to the robotic arm. The probe was held perpendicular over the Z-phantom to facilitate the U.S. scan plane intersection with Z-fiducials (Fig. 4) and to minimize the blurry effect that the finite thickness of the U.S. beam has on images. Then, transducer motions were taught to the robotic arm to locate the Z-fiducial markers while acquiring U.S. images.

Because peripheral arteries in lower limbs have a 3–8 cm depth range,³⁵ operator-dependent adjustments of U.S. image settings are required for a given scan. Consequently, such settings were evaluated because of the impact on calibration transforms.^{17,36} The U.S. image acquisition parameters included four depths (5, 6, 7, and 8 cm) at no zooming, with a fixed focus depth of 4–5 cm, and three focus beam depths (2–4, 4–5, and 5–7 cm) at a fixed 7 cm depth with no zooming. The focus beam depth provides the best lateral resolution of the U.S. transducer to distinguish small adjacent structures perpendicular to the beam's major axis. At the 7 cm depth, with the best focus beam depth that had previously been found, three amplifications (i.e., zooms), corresponding to window sizes of 2, 3, and 4 cm, were also used. The zoom

setting of the U.S. scanner allows the display of only a selected region of interest remote from the transducer, where a smaller window size represents a higher magnified ROI. For each setting, ten U.S. scans were acquired, and, for each scan, ten frames were selected to compute 10 calibration transforms. The ROI was cropped and visible Z-fiducials identified and segmented manually.

II.B.2. Calibration equations

Different coordinate systems are involved in the calibration procedure and each one is related to the others by Eq. (1) (Fig. 4). Every transformation matrix T contains three rotations (α, β, γ) and three translations (x, y, z). The standard notation throughout this manuscript is ${}^A T_B$, where the coordinate system B is defined into the referential A .

$$\begin{pmatrix} x_k \\ y_k \\ z_k \\ 1 \end{pmatrix} = {}^Z T_R \cdot {}^R T_P \cdot {}^P T_I \cdot \begin{pmatrix} s_x \cdot u_k \\ s_y \cdot v_k \\ 0 \\ 1 \end{pmatrix}. \quad (1)$$

In the above equation, ${}^Z T_R$ is the unknown transformation of robot referential R into the Z-phantom, ${}^R T_P$ represents the known transformation of U.S. probe P into robot referential R for an acquired image, and ${}^P T_I$ is the unknown calibration transformation of image I in U.S. probe P . For each image, k , u_k , and v_k are column and row indices with respect to the B-scan origin; s_x and s_y are scaling parameters in mm/pixel, estimated from B-scan depth and zoom settings. Thus, a point in the k th U.S. image is localized in the Z-phantom referential with x_k , y_k , and z_k .

II.B.2.a. Identification of Z-fiducials. U.S. images depicted multiple dots that could be used to identify Z-fiducials (see Fig. 3). Each feature point in an U.S. image I were identified in the Z referential by trigonometry, an approach similar to that in Ref. 31. In particular, when the U.S. image

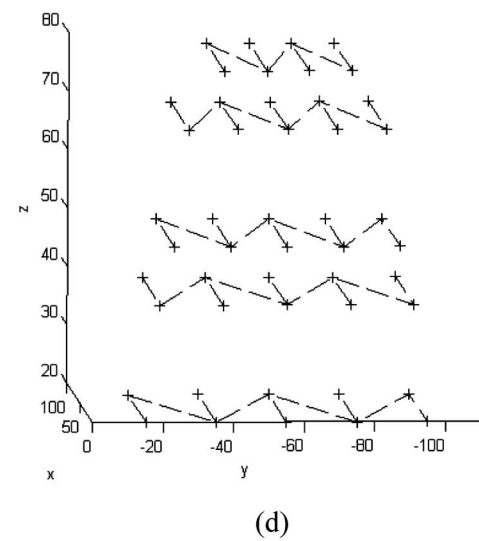
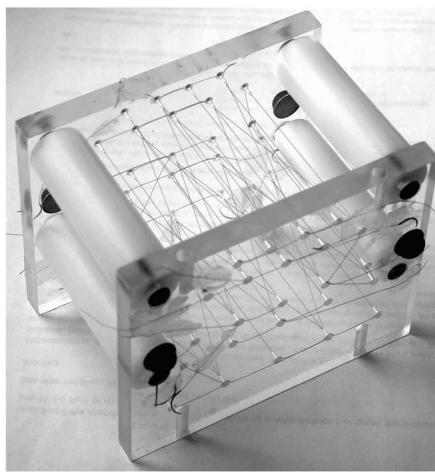
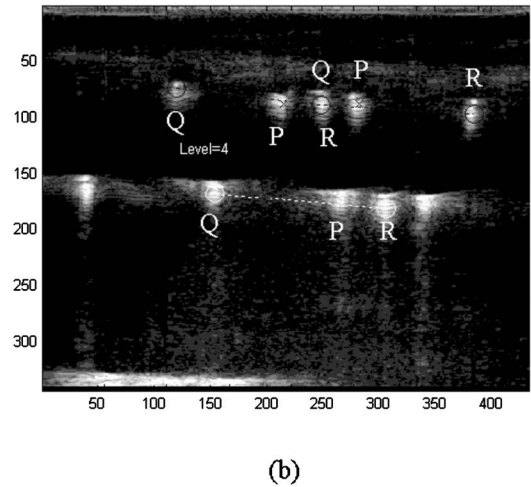
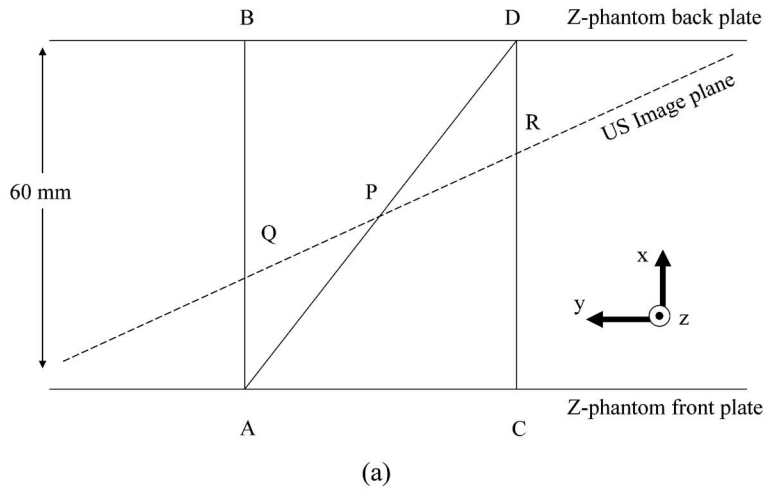


FIG. 3. (a) Top view of the Z-phantom that illustrates a single Z-fiducial (i.e., segment wires \overline{BA} , \overline{AD} , and \overline{DC}). An U.S. plane (i.e., dashed line) intersects these wires in collinear points Q , P , and R . (b) Example of an U.S. image that contains multiple points of Z-fiducials in its field of view. (c) Side view of the complete Z-phantom is shown with (d), a grid of the entire 19 Z-fiducials constructed.

plane intersects the Z-shaped phantom wires, it forms multiple collinear points similar to \overline{QPR} (see Fig. 3) in the U.S. image. Usually, these crossings are unknown in the Z referential. However, while not visible in the U.S. image, the A , B , C , and D location points are known in the Z referential due to the manufacture of Z-fiducials (Fig. 3). Thus, with similar triangles Δ , it was possible to calculate the location of the homologous point P that expresses the location of image plane I in the Z-phantom. The following equations are derived from the similar ΔAPQ and ΔDPR that define point P :

$$x_P = x_A + h \cdot (x_D - x_A), \tag{2}$$

$$y_P = y_A + h \cdot (y_D - y_A), \tag{3}$$

$$z_P = z_A + h \cdot (z_D - z_A), \tag{4}$$

where h is the ratio of distance \overline{AP} to distance \overline{AD} that is equivalent to the ratio of distance \overline{QP} to distance \overline{QR} . By

identifying the location of point P inside the U.S. image plane I (Fig. 3), this corresponds to the detection of the same feature location point in the Z-phantom referential [i.e., x_k , y_k , and z_k in Eq. (1)]. In practice, several Z-fiducials were localized within a given U.S. image plane to determine the relative position and orientation of the scan.

II.B.2.b. Localization of the Z-phantom. A calibration procedure with a spherical pointer that fits tightly into the robot markers of Fig. 2 was first used to localize the Z-phantom in the robot referential R . A complete description of the method appears in Ref. 24. For each robot marker, ten independent sets of points corresponding to different articulations of the robotic arm were taught, then replayed and recorded by the robotic system. An iterative closest point (ICP) algorithm with Delaunay tessellation was employed to fit the measured robot points to the real Z-phantom robot marker point coordinates (MATLAB open source code ICP, version 1.4, by Per Bergström, March 7, 2007). Thus, rigid body transformation

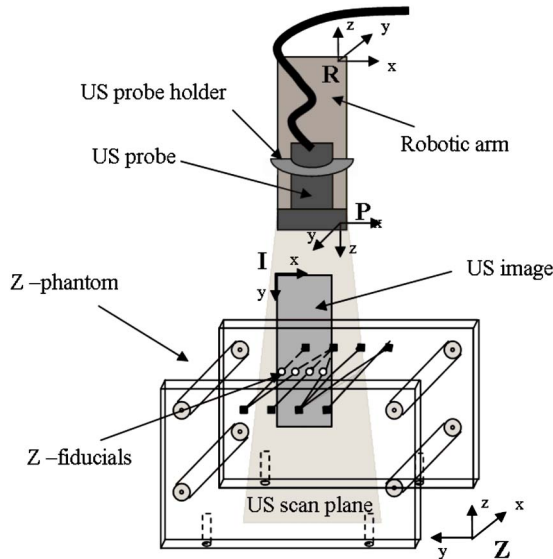


FIG. 4. The coordinate system involved in the calibration method: Z-phantom Z, U.S. image I, U.S. probe P, and robot R. The calibration transform was determined from a series of coordinate frame transformations that relate Z features to I and R.

zT_R between the Z-phantom model and the robot marker points could be determined with this method.

II.B.2.c. Calibration algorithm. A calibration algorithm served to determine the calibration transform that defines the spatial relationship between U.S. image I and U.S. probe P. Equation (1) presents an overdetermined system of nonlinear homogeneous equations where most of the Z-phantom parameters can be estimated. The remaining unknown parameters, i.e., the calibration transform of image I into U.S. probe P (PT_I), were computed by the Levenberg–Marquardt iterative algorithm, with a detailed description provided in Refs. 17 and 30.

II.B.3. Calibration performance evaluation with the Z-phantom

The precision of the calibration procedure was evaluated by measuring variations in the x - y position of the U.S. image plane due to spatial calibration errors.²⁶ It is not a measure of accuracy of the calibration parameters but of their repeatability. Ten different U.S. images of the Z-phantom were assessed: Six fiducial markers in each image were identified and reconstructed into the phantom referential with the calibration transform of Eq. (1). The precision of calibration C_{rms} was computed by

$$C_{\text{rms}} = \frac{1}{\sqrt{MN}} \sum_{i=0}^M \sum_{j=0}^N \sqrt{(x - \bar{x})_{i,j}^2 + (y - \bar{y})_{i,j}^2}, \quad (5)$$

where $(x - \bar{x})_{i,j}$ is the variation from the mean location \bar{x} for fiducial positions i in the x direction for image j [see Fig. 4 for the identification of the image coordinate system $I(x, y)$]. This definition applies as well to direction y . For every U.S. image setting (i.e., depth, focus beam depth and zooming), ten calibrations (i.e., ten measures of C_{rms}) were performed

to obtain the mean precision that was calculated with $M=6$ fiducial markers and $N=10$ U.S. images. The total sample size thus corresponded to the identification of 600 points on the Z-phantom. Note that this is the same equation as Eq. 8 in Ref. 24 but with a different notation.

II.C. 3D reconstruction performance evaluation on a lower limb-mimicking artery

II.C.1. Vascular phantom geometry and experimental setup

A phantom, mimicking a lower limb femoral artery, was fabricated to evaluate the 3D reconstruction performance of the robotic scanner. It contained two axisymmetrical stenoses of 80.0% (S1) and 75.0% (S2) in area reductions with a “disease-free” diameter of 7.87 ± 0.11 mm (i.e., gold standard dimension). The vessel central axis was positioned at 3.4 cm from the top of the phantom. The entire fabrication process, characteristics, and geometric accuracy of the vessel lumen embedded in this phantom are available in Ref. 37. The mathematical model describing the vessel lumen geometry can be found in Ref. 38. This geometry served as the gold standard reference for all subsequent measures that follow.

The vascular phantom was fixed tightly into the robot workplace and scanned along its length. A quasiparallel plane U.S. scan path was taught and replayed by the robot and B-mode images were acquired at the same settings as those used for precision assessment with the Z-phantom (i.e., four depths, three focus beam depths, and three zooms). For each U.S. image setting, ten scans were captured to reconstruct ten vessels in 3D.

II.C.2. 3D-U.S. reconstruction process

At first, the vessel lumen of every U.S. scan was segmented with a fast-marching method based on gray level statistics and gradients adapted from Ref. 39. Each pixel of the segmented lumen contour was then mapped into the robot referential with the best calibration transform computed and the corresponding probe positions. The transformed lumen contours were resampled on a 300×20 rectangular grid and interpolated to provide a 3D surface rendering of the reconstructed vessel. After that, the reconstructed polygon models were transformed to generate contours normal to the vessel center axis, as in Ref. 40.

II.C.3. 3D reconstruction performance evaluation

The accuracy of 3D reconstructions was assessed by determining lumen surface map and vessel area errors from cross-sectional planes along the 3D-reconstructed vessel. Reconstructed and gold standard model-matching were performed by finding the center of gravity of both 3D vessel lumens and by computing the appropriate transformation matrix (translation and rotation) that minimized the difference between both referential systems. Lumen surface map error

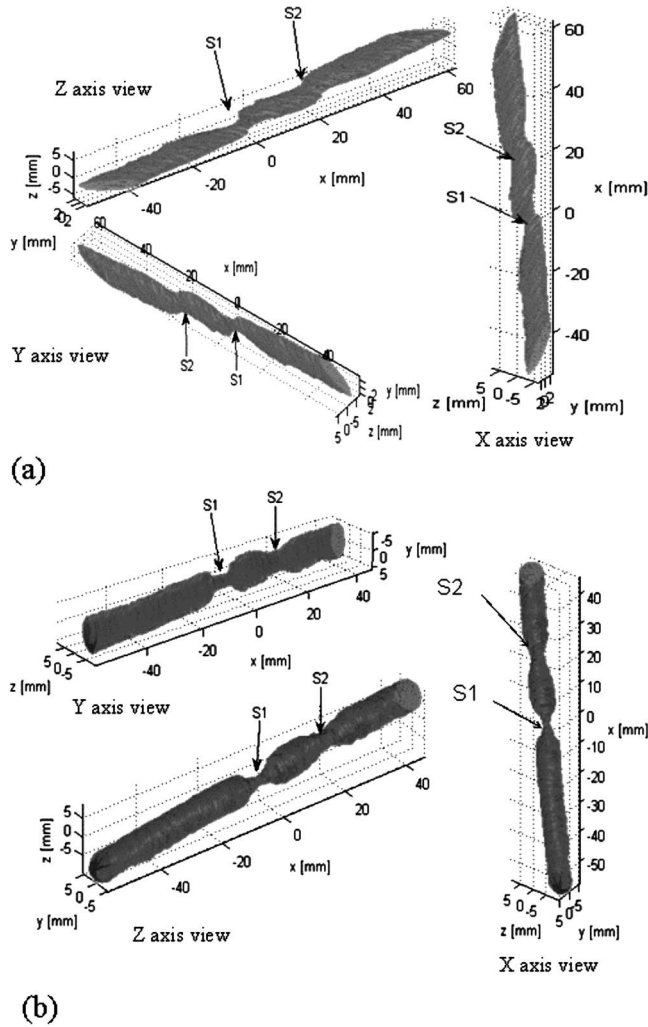


FIG. 5. Examples of 3D-reconstructed vascular geometries with axisymmetric double stenoses (S1 and S2). (a) The worst 3D vessel reconstruction is displayed at 7 cm image depth and 4–5 cm focus beam depth with no zooming. (b) The best 3D reconstruction is obtained at 7 cm image depth, 4–5 cm focus beam depth, and 3:7 zoom setting.

was evaluated by measuring the absolute distance between the reconstructed geometry and that of the gold standard vessel, as expressed by

$$E_{i,j,k} = \text{abs}(M(i,j,k) - S(i,j,k)), \quad (6)$$

where M is the surface map of the reconstructed vessel, S is the surface map of the gold standard vessel, $1 \leq i \leq X$ where X is the number of grid points along the x axis depicted in Fig. 5, $1 \leq j \leq Y$ where Y is the number of grid points along the y axis, and $1 \leq k \leq Z$ where Z is the number of grid points along the z axis.

For each reconstruction, the error in area was also evaluated with a polygon-specific function of MATLAB, *Polyarea*, which computes the average number of pixels inside a closed contour. Thus, for each U.S. image setting where ten reconstructions were performed, these measures (surface map and area errors) were tabulated independently into one mean (sample sizes= $X \times Y \times Z$ for the surface map accuracy and X

TABLE I. Calibration precision. C_{rms} is the reconstruction precision of the medical robotic system evaluated with Eq. (5) for different U.S. image settings. N is the total number of sample points used.

U.S. image parameters	Settings	C_{rms} (mm)	Sample size (N)
Image depth at fixed 4–5 cm focus beam depth and no zoom	5 cm	1.19 ± 0.91^a	600
	6 cm	0.93 ± 0.47^a	600
	7 cm	0.60 ± 0.38	600
	8 cm	0.58 ± 0.36	600
Focus beam depth at fixed 7 cm image depth and no zoom	2–4 cm	0.72 ± 0.41	540
	4–5 cm	0.67 ± 0.32^b	600
	5–7 cm	0.78 ± 0.37^a	600
Zoom at fixed 7 cm image depth and 4–5 cm focus beam depth	2:7	0.47 ± 0.27^a	600
	3:7	0.75 ± 0.41	600
	4:7	1.10 ± 0.60	600

^aIndicates a statistically significant difference on pairwise comparisons between settings on a U.S. image parameter with $p < 0.001$.

^bSignifies $p < 0.05$.

for the area accuracy, where X also corresponds to the number of cross-sections).

III.D. Statistical analysis

Analysis of variance with multiple pairwise comparisons by the Bonferroni method was performed on the calibration and 3D-reconstruction results to evaluate differences among U.S. imaging settings. All statistical analyses were done with the SPSS statistical software (version 13.0, SPSS Inc., Chicago, IL).

III. RESULTS

III.A. Calibration performance evaluation with the Z-phantom

Table I presents calibration precisions C_{rms} achieved with the robotic scanner. At four different image depth settings (i.e., from 5 to 8 cm), fixed focus depth of 4–5 cm, and no zooming, precision improved as the U.S. image depth was increased (C_{rms} varied from 1.19 to 0.58 mm); 5 and 6 cm had significantly lower precision than other depths ($p < 0.001$). At the fixed image depth of 7 cm and no zooming, C_{rms} varied from 0.67 to 0.78 mm as a function of focus beam depth, 5–7 cm being the poorest ($p < 0.001$) and 4–5 cm, the best ($p < 0.05$). Note that a smaller sample size served to determine calibration performance at the 2–4 cm focus beam depth because not enough Z-fiducials were visible to localize the U.S. plane on some scans. At the same 7 cm fixed depth and the best focus beam depth of 4–5 cm, optimum mean precision was achieved at maximum zooming (2:7) ($p < 0.001$) and degraded with less magnification (precision varied between 0.47 and 1.10 mm).

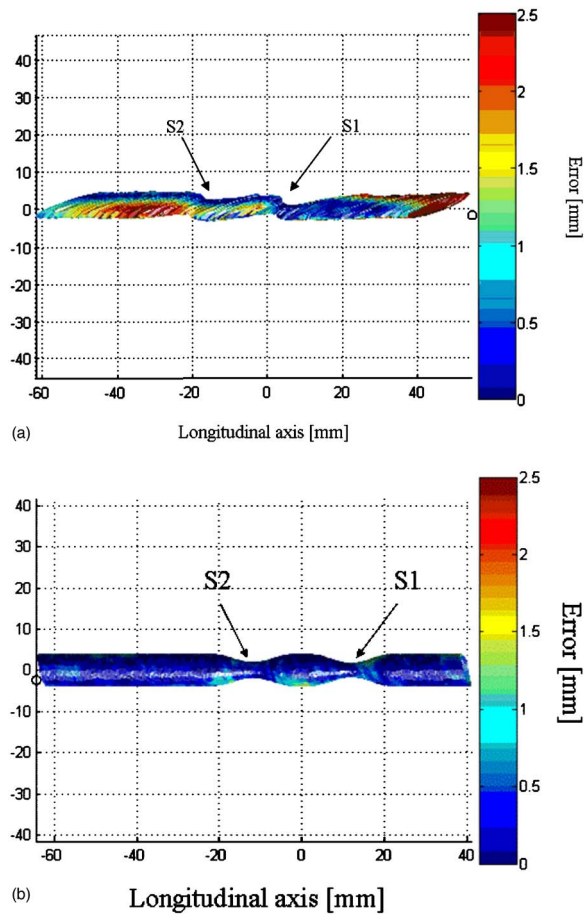


FIG. 6. Reconstruction errors with respect to the axisymmetric cylindrical gold standard model. (a) Error map of the worst reconstruction corresponding to panel a of Fig. 5. (b) Error map of the best reconstruction corresponding to panel b of Fig. 5. Note that the same projected view is used on both panels; differences are associated with reconstruction errors.

III.B. 3D reconstruction performance evaluated on a lower limb-mimicking artery

Figure 5 presents examples of the worst (panel a) and best (panel b) 3D reconstructions at different views with labeled stenoses. In Fig. 5(a), vessel shape showed large distortions, whereas in Fig. 5(b), overall geometry appeared to be acceptable. Corresponding lumen surface map errors are reported in Fig. 6. Note that similar distance errors were found for the nine other reconstructed lower limb-mimicking vessels at the specified U.S. image settings. Table II summarizes the accuracy of all 3D reconstructions. The best reconstructions were obtained at the 3:7 zoom setting for an image depth of 7 cm and a focus beam depth of 4–5 cm [0.40 ± 0.03 mm, Fig. 6(b)] ($p < 0.05$). No vessel reconstructions were computed at the 5–7 cm focus beam depth because we assumed that worse results would be obtained (because the focal depth was the farthest with respect to the vessel central axis depth of 3.4 cm).

Figure 7 shows the reconstructed vessel areas at all tested U.S. image parameters (legends indicate comparisons with significant differences, $* p < 0.05$). In general, an underestimation of cross-sectional areas was noted, except for the best

TABLE II. Reconstruction accuracy of the medical robotic system evaluated in terms of distance errors for different U.S. image parameters. Each value represents the mean \pm standard deviation computed over one reconstruction from N total number of models used. Each pair of multiple comparisons between settings of U.S. image parameters was significantly different ($p < 0.05$).

U.S. image parameters	Settings	Reconstruction error (mm)	Sample size (N)
Image depth at fixed 4–5 cm focus beam depth and no zoom	5 cm	0.87 ± 0.08	7
	6 cm	1.20 ± 0.02	10
	7 cm	1.74 ± 0.08	10
	8 cm	1.45 ± 0.12	10
Focus beam depth at fixed 7 cm image depth and no zoom	2–4 cm	1.71 ± 0.03	10
	4–5 cm	1.11 ± 0.003	10
Zoom at fixed 7 cm image depth and 4–5 cm focus beam depth	2:7	0.93 ± 0.04	9
	3:7	0.40 ± 0.03	10
	4:7	0.46 ± 0.03	10

setting in panel c (3:7 zoom) where the vessel geometry was adequately reconstructed. In 6, 7, and 8 cm image depth settings, at a fixed focus beam depth and no zooming, significantly underestimated areas were found ($p < 0.05$) [Fig. 7(a)], whereas in focus beam depth settings at a fixed image depth and no zooming, the areas revealed no statistical difference ($p = 0.11$) [Fig. 7(b)]. In zoom settings at fixed depth and focus beam depth, differences were generally in the most underestimated areas: 2:7 and 4:7 ($p < 0.05$).

IV. DISCUSSION

IV.A. Calibration performance evaluation

In this study, for all image settings, the mean C_{rms} calibration precision ranged from 0.47 to 1.2 mm (Table I). This indicates that the calibration transform is variable from one U.S. image setting to another and that parameters can be adjusted on U.S. scanning equipment to improve C_{rms} . However, some scanner parameters that may affect C_{rms} could not be improved or modified, such as the axial, lateral, and elevational resolutions that, respectively, depend on the wavelength propagating in the medium (U.S. frequency), on beam focusing, and transducer lenses shape. Such parameters were not specifically considered in our study but their impact on C_{rms} can be approximated, according to a study realized using a similar scanner with a linear array probe of 10 MHz.⁴¹ In that study, reported U.S. image resolution was 0.3–0.4 mm in axial, 1.0–2.0 mm in lateral, and 3.0–4.0 mm in elevational at a 3.0 cm depth. It is clear that the use of an U.S. scanner with better resolutions would have positively impact our results, especially lateral and elevational resolutions. Nevertheless, these are typical parameters of modern U.S. scanners.

As also noted, each adjusted parameter (image depth, focus beam depth, and zooming) individually impacted the precision of the 3D robotic U.S. scanning system. For the image depth setting with no zooming at a fixed 4–5 cm focus beam depth, C_{rms} was minimum at either 7 or 8 cm with a mean

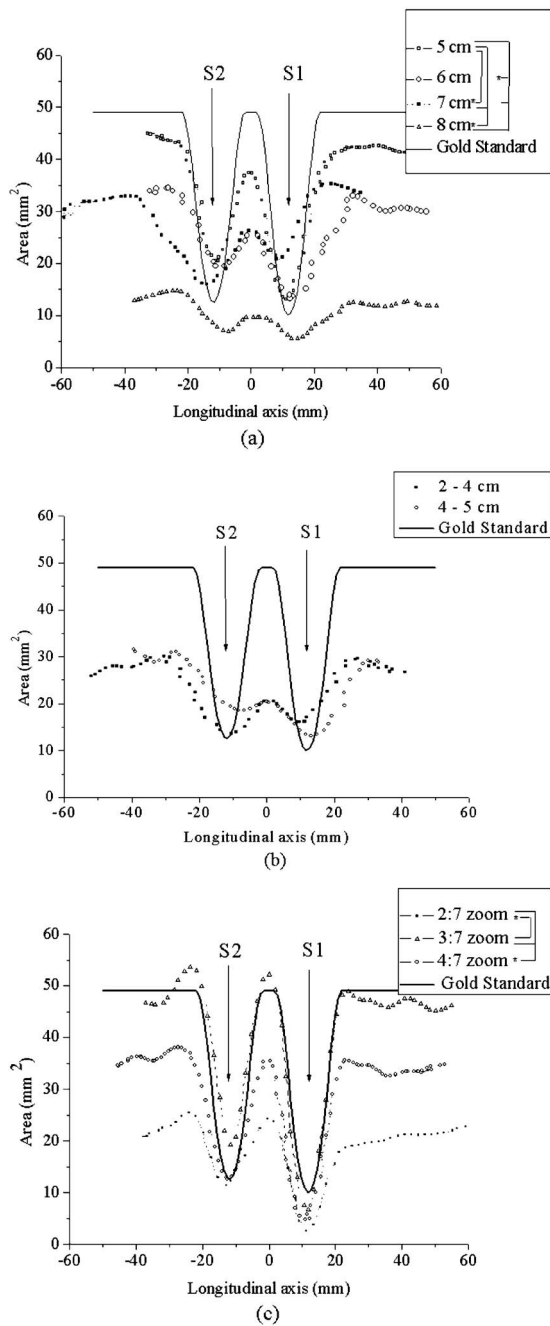


FIG. 7. Mean areas of 3D-reconstructed vascular geometries with respect to gold standard dimension at different U.S. image settings (for each curve, standard deviations between reconstructions are not displayed to facilitate reading): (a) At four image depths, 4–5 cm fixed focus beam depth, and no zooming; (b) at a fixed image depth of 7 cm, no zooming, and two focus beam depths; and (c) at 7 cm fixed image depth, 4–5 cm fixed focus beam depth, and three zoom settings. For each panel, * indicates a statistically significant difference between U.S. settings on pairwise comparisons with $p < 0.05$.

value close to 0.60 mm (no statistical differences were noted between both measures). This result was not anticipated since C_{rms} performance was expected to become poorer as U.S. image depth increased^{27,29,42} because pixel density (i.e., axial and lateral) decreased.

In addition to the U.S. scanner parameter selection, variations in the calibration transform were found dependent on points chosen in the B-scan. A greater number of points from the Z-phantom provided a more defined plane that could result in better calibration precision. Thus, at the smallest depth settings, lower precisions can be attributed to the limited field of view of the Z-phantom in U.S. images, giving less Z-fiducials available for establishing the calibration transform of Eq. (1). Other studies with Z-phantoms have also found improved calibration precision at deeper U.S. image settings for the same reason.^{31–34} In the case of the focus beam depth and referring to Figs. 2 and 3, the best C_{rms} performance was achieved at the 4–5 cm setting (0.67 ± 0.32 mm), which corresponds to the mid depth of the Z-phantom with a dimension of 9 cm. Accordingly at this setting, more Z-fiducials with optimum resolution could be imaged, thus improving the calibration transform. As also seen in Table I, the zoom amplification ratio of 2:7 provided the best precision, with $C_{\text{rms}} = 0.47 \pm 0.27$ mm. Image quality and definition were maximized with zooming and enhanced the calibration precision. However, for the calibration transform to be estimated adequately with zooming, care had to be taken to note the (x, y) position of the zoomed ROI within the whole U.S. scan plane.

We also noted in this study that it was difficult to align the scan plane with the Z-fiducials because the finite U.S. beam thickness (elevational resolution) caused point targets to appear in the B-scan even if they were not exactly in the mid position of this scan dimension.³² Thus, dots that resulted from the intersection of Z-fiducials with the scanning beam appeared as smeared ellipses. This U.S. beam offset could render the segmentation of Z-fiducials challenging in B-scans and affect C_{rms} . In summary, the most repeatable calibration transform should be identified before scanning a vessel and this requires testing different U.S. image settings. Nevertheless, the results do not guarantee accurate reconstruction of a lower limb artery because this measure only represents the consistency of the calibration parameters and not their accuracy.

IV.A.1. Comparison with the literature

Calibration precision provides a measure that allows a fair evaluation of 3D-U.S. system advantages and limitations. Previous Z-phantom studies with 3D-U.S. freehand systems have reported similar findings as our 0.60 mm root mean square (RMS) (600 measures) calibration precision at 7 cm U.S. image depth, no zooming, with a 10 MHz linear array.^{31–34} Precisions of 1.0–4.5 mm and 1.0–2.0 mm RMS (20 image samples each) have been obtained for the electromagnetic sensor system at, respectively, 9 and 16 cm U.S. image depths with a 3.5 MHz sector-phased array.³² For the optical tracking system, precisions of 0.7 and 1.2 mm (ten image samples each) have been presented for U.S. image depths of 8 and 15 cm, respectively, using a 3.75 MHz curvilinear probe.³³ Still, other similar studies with a 7.5 MHz curvilinear probe have found this measure to deteriorate to 1.6–2.7 mm (36 measures) between 6 and 12 cm U.S. image

depths,⁴³ or, alternatively, to improve to 1.04 ± 0.84 mm (1830 measures) with a 10 MHz linear probe array.³¹ While our results seem to perform better than these previous studies (especially when zooming is considered), comparison between other reports should be undertaken with caution because differences do exist in the U.S. echograph, probe frequency, image settings, 3D tracking device, and performance evaluation method utilized. In comparing precision for different 3D-U.S. calibration methods,¹⁷ smaller values were obtained when it was computed as the residue of the nonlinear minimization problem of Eq. (1),^{30,34} or, alternatively, when it was assessed as an average measure^{26,31,33,43} rather than a RMS. It is noteworthy that most recent studies in 3D-U.S. calibration present calibration precision as an average metric; our results would definitely be artificially improved if they were computed this way.

Calibration precision also depends on probe motions. It has been shown that acquisitions by linear translation of the probe give significantly better precision than acquisition by titling,³¹ which is a difficult task to achieve in freehand tracking. In addition, the reproducibility of calibration is limited in freehand. To ensure reproducible 3D-U.S. freehand results, a pivoting cradle for mechanical sweeping was even incorporated into the probe calibration procedure in Ref. 34. The robotic scanner has the advantage of being repeatable in scanning paths for U.S. image acquisitions.^{24,44} This key feature is what permitted the in-depth analysis of U.S. image parameters to characterize calibration performance.

Another benefit in this study is our adaptation of the Z-phantom with micrometer size non-water-absorbable material wire (i.e., polypropylene). Previous studies showed drawbacks in identifying Z-fiducials in U.S. images.^{32,33} Smaller wires (i.e., 0.2 mm diameter), higher frequency probes (i.e., 10 MHz),³¹ or mounting a thin rubber membrane on top of the Z-phantom were thought to improve this task.³³ Better calibration precision was achieved in our study compared to prior works.

In the literature on robotics, calibration precision can be compared to a limited number of studies. Using the same 3D-U.S. robotic system and a 10 MHz U.S. linear probe at a 6 cm U.S. image depth, an improvement in precision to 0.93 mm RMS (600 observations) has been obtained with the Z-phantom compared to the X-wire calibration method that allowed us to obtain a 3.5 mm RMS precision (76 observations).²⁴ Moreover, our system showed a better precision at 0.58 ± 0.36 mm RMS (600 observations) for a 8 cm U.S. image depth compared to another robotic system evaluation with a plane wire calibration method that achieved 1.23 ± 0.65 mm (780 observations)²⁵ mean precision with a 14 MHz linear array probe at the same image depth of 8 cm.

Some disadvantages exist with the Z-phantom calibration procedure. Our method was tedious because segmentation of wires was manual and images contained speckle noise. Automatic segmentation methods of Z-fiducial collinear points in predefined search regions have already been developed, but these approaches are known to have larger variations than a manual operator.^{31,33} These promising algorithms

could enhance the efficiency of Z-phantoms if segmentation becomes more robust. Also, errors are introduced into the calibration performance when the medium (polypropylene wires immersed in water) has a different speed of sound than human tissues (1540 m/s) assumed by the U.S. scanner.^{17,33} The speed of sound impact on calibration has not been explored in this study because we judged it to be minimal.

Finally, in this work, we have demonstrated that satisfactory results could be achieved with a Z-phantom to calibrate a 3D-U.S. imaging robot. Precisions favorably comparable to other studies have been obtained for different U.S. image settings. In clinical practice, the calibration procedure needs to be fast and repeatable. To improve efficiency, this calibration procedure should be performed only once to characterize U.S. image settings that match the target clinical application. A special adapter that ensures repetitive and precise attachment between the robot handle and the U.S. probe should be conceptualized for this purpose. Also, a robust automatic segmentation algorithm should be used with typically gel-based agar incorporated into the Z-phantom to reduce U.S. image artifacts due to possible reverberation. Another alternative would be to use raw digital radiofrequency signals^{45,46} instead of B-mode images to improve segmentation. However, this would require further hardware and software developments into the 3D-U.S. robotic system and postprocessing of RF signals.

IV.B. 3D reconstruction performance evaluation on a lower limb-mimicking artery

In this study, reconstruction accuracy to represent a 3D vessel geometry was evaluated between 0.40 and 1.74 mm (Table II) with significant differences observed for all U.S. image settings investigated. Vessels reconstructed were more accurate at smaller depths (0.87 ± 0.08 mm) even if the calibration transform used provided less precision under these conditions (Table I). This can be attributed to the higher pixel density around the vessel at smaller depths; the disease-free vessel lumen covered a range from 3 to 3.8 cm within the phantom. According to Table II, the optimum reconstruction was obtained by placing the focus beam depth slightly below the vessel at 4–5 cm. Reconstruction accuracy was the best when the depth setting of 7 cm was zoomed at 3:7 (0.40 ± 0.03 mm). This result was not anticipated, as the highest magnification 2:7 zoom was expected to provide the best reconstruction accuracy because the optimum precision of 0.47 mm was obtained for these settings. Poorer accuracy can be produced by U.S. image artifacts becoming larger with zooming.

Area is another measure that we used to express the accuracy of the 3D vessel geometry. Most area profiles showed underestimations with two axisymmetric stenoses spaced apart at approximately the same distance for different U.S. image settings (Fig. 7). This information reveals distortions in vessel shape where an oval and near elliptical geometry could be reconstructed. At 7 cm depth, 4–5 cm focus beam depth, and 3:7 zoom setting, reconstructed vessels showed

the best fidelity to the circular gold standard geometry. These observations reflect reconstructed accuracies of Table II.

Overall, errors in vessel representations are attributed to the phantom fabrication process, segmentation of U.S. images, robot intrinsic performance, and to the reconstruction procedure. First, the fabrication process of the vascular phantom has -1.4% error in diameter.³⁷ This small contribution may nevertheless be important because the gold standard geometry was based on this model. Second, the segmentation algorithm used to detect the vessel lumen was adapted from a method implemented for IVUS images.³⁹ The segmentation accuracy in our images remains unknown and not comparable to IVUS reports. A slight error of a few pixels in segmentation can translate into errors of some mm in 3D vessel representation. Third, another contributor to the vessel reconstruction quality is the robot performance in localizing an object in space. As reported earlier,²⁴ our robot has a positioning accuracy of $0.46\text{--}0.75$ mm that is repeatable at 0.20 mm and an interdistance accuracy of $0.26\text{--}0.61$ mm. Among these performance measures, only the x , y , and z interdistance accuracy can be compared to reconstruction errors reported in Table II ($0.40\text{--}1.74$ mm). As expected, reconstruction errors were slightly larger than the robot interdistance accuracy because the former measure includes all together the abovementioned contributing uncertainties (i.e., phantom, segmentation, and reconstruction performances). Because 3D vessel reconstructions were coregistered with the gold standard vascular phantom geometry before assessing errors of Table II, the robot positioning accuracy and repeatability are less relevant in this discussion. Lastly, and to conclude this section, we support the hypothesis that the reconstruction procedure was the main source of error of Table II because it derives directly from the accuracy of the calibration transform [Eq. (1)].

IV.B.1. Comparison with the literature

The 3D lower limb-mimicking artery was evaluated for different calibration transforms. Performance was assessed in terms of distance (reconstruction) accuracy and areas. Other similar calibration studies but with different calibration methods (i.e., X-wire, wall, three-wire, Cambridge phantom, etc...) also examined performance of 3D-U.S. systems in distance accuracy but only on 1D or 2D reconstructed feature-based target points from the calibration phantom itself or from a simple independent geometric object (e.g., balloon or pin heads). We summarize their results relative to our $0.87\text{--}1.74$ mm 3D vessel reconstruction accuracy obtained for the $5\text{--}8$ cm U.S. image depths, fixed $4\text{--}5$ cm focus beam depth, and no zooming (Table II). Recall that our findings were obtained with a 10 MHz linear array probe for ten vessel reconstructions (approximately 6000 points per reconstruction).

Z-phantom studies with an electromagnetic freehand tracking and a 3.5 MHz phased array have reported 0.23 ± 2.89 mm distance accuracy for 960 intersteel bead measurements at 9 cm U.S. image depth,³² whereas inter-Z-fiducial analyses using optical freehand tracking devices with

a 10 MHz linear array probe had 1.15 ± 0.43 mm distance accuracy for 810 measurements at 8 cm U.S. image depth.³¹ Other Z-phantom studies report results for intertargets and feature length measurement accuracy between 0.2 and 1.2 mm with optical systems and probes ranging from 3.5 to 7.5 MHz at $6\text{--}12$ cm U.S. image depths with less than 30 samples.^{34,36,43}

Moreover, alternative phantom calibration methods (i.e., X-wire, wall, three-wire, Cambridge phantom, etc...) with electromagnetic and optic freehand tracking devices in the literature have intertarget distance accuracies that range from -0.19 μm to 3.0 mm.^{17,26,28–30,33} Of course, it is not possible to directly compare the accuracy of all these studies to our results because many differences exist in calibration phantoms, U.S. probe frequencies, U.S. image settings, and distance accuracy metrics.

Generally, performances of our calibrations for accurate vessel reconstructions are of similar magnitude as the intertarget distance accuracy reports of 3D-U.S. optical systems (best positional accuracy¹⁷). Electromagnetic systems seem to show significantly better results in intertarget distance accuracy than other systems. However, most of these reported measures in the literature are misleading because unsigned values are computed into their average, thus improving their overall accuracy. Also note that valid clinical 3D-U.S. system accuracy cannot be extrapolated from these intertarget measures because they have no relation to the clinical context aimed.

Studies performed in clinic with 3D-U.S. freehand systems have preferred to directly show the clinical potential of their technologies for monitoring human vessel pathologies over time.^{47–50} Because most studies have not validated their 3D reconstruction with a gold standard, the validity of their 3D systems to accurately represent a 3D geometry is unknown, and if they did,⁵¹ no information is available to assess the calibration method used and its performance. Consequently, diseased vessels can be misdiagnosed when unidentified systematic errors intermingle with the pathology in their 3D representations.

Also, our study has the advantage of being comparable to two others that employed a similar vascular phantom and the same U.S. scanning equipment and probe. In the first investigation, the accuracy to reconstruct vascular phantom diameters varied between -0.37 and -0.90 mm at 6 cm U.S. image depth with a previous X-wire calibration method and the same 3D-U.S. robotic imaging system.²⁴ In our experiment, reconstruction accuracy was 1.20 mm at this particular depth. The results varied between studies because of the way measurements were assessed. In Ref. 24, the diameter at specific cross-sections of the 3D representation was taken into account and evaluated on gold standard geometry with microcaliper measures (unsigned errors). In the current paper, entire points of surface reconstruction were assessed on gold standard geometry and ten reconstructed samples were computed for the mean measure. Evidently, the present report is more rigorous than our previous work in Ref. 24 to validate the 3D-U.S. imaging robotic system. The second study, with similar vascular phantoms, evaluated in-stent restenoses *in*

vitro with an electromagnetic system and a linear step motor for 3D reconstructions.⁵² A value of 1.0 ± 0.1 mm RMS calibration accuracy was achieved with the STRADWIN software at 4.5 cm U.S. image depth with no available information on zooming and focus beam depth. Our system showed better results with 0.87 ± 0.08 mm reconstruction accuracy at 5 cm U.S. image depth. However, the *in vitro* in-stent restenoses study provided no information relative to precision analysis of calibration parameters. Thus, their suggestive results remain inconclusive and not equivalent.

The goal of calibration is to find the correct (or optimum) transform that allows 3D geometry to be reconstructed accurately. Our study attained this objective by evaluating the performance of different U.S. image settings that affect calibration transformation accuracy to reconstruct a 3D lower limb-mimicking artery. Our validation was the first of its kind for lower limb 3D-U.S. vessel reconstruction. In this work, reconstruction errors and cross-sectional areas completely allowed the quantification and identification of distortions obtained with the robotic scanner on our 3D vessel representations. Future analyses will include the reconstruction of complex lower limb arterial geometries, multimode imaging comparisons, stenosis quantification, and a possible clinical study to demonstrate the benefits of this robotic scanning system.

V. CONCLUSION

The 3D-U.S. robotic scanner was validated to adequately reconstruct a 3D lower limb-mimicking artery. A Z-phantom calibration procedure was completed with this robotic system and, as a result, calibration transforms were characterized with U.S. image settings according to precision and 3D reconstruction accuracy. Calibration precision was found to perform best at deeper U.S. image settings with focus beam depths corresponding to target Z-fiducials located on the U.S. scan and at the highest zoom. Reconstruction accuracy was evaluated in terms of distance accuracy with respect to a gold standard geometry of a vascular phantom. The cross-sectional area was also analyzed along the length of the reconstructed vessels. Optimum U.S. settings to accurately reconstruct the vessel were at lower U.S. image depths, a focus beam depth slightly below the vessel, and a mid-sized window zoom to reduce artifacts. These results are likely suitable for the clinical evaluation of stenoses. Further developments and validations of the robotic system are nevertheless necessary to provide a platform that would meet clinical needs.

ACKNOWLEDGMENTS

This work was supported in part by the Canadian Institutes of Health Research (CIHR) under Grant No. MOP 53244. Dr. Soulez is recipient of a National Scientist Award of the Fonds de la Recherche en Santé du Québec (FRSQ). Ms. Janvier is the recipient of studentship awards from the Fonds de la Recherche sur la Nature et les Technologies du Québec, TD Canada Trust, the Institute of Biomedical Engineering at Université de Montréal, the Quebec Black Medi-

cal Association, and the End of Study Grant from the Faculty of Graduate and Postgraduate Studies at Université de Montréal. The authors are grateful to Ms. Zhao Qin, Mr. Boris Chayer, Dr. Marianne Fenech, and Dr. Marie-Hélène Roy Cardinal for technical support. The authors are grateful to Mr. Ovid M. Da Silva for manuscript editing.

^{a)}Electronic mail: majanvier@gmail.com

^{b)}Author to whom correspondence should be addressed. Electronic mail: guy.cloutier@umontreal.ca; Telephone: (514) 890-8000 Ext: 24703; Fax: (514) 412-7505.

¹A. Stoyioglou and M. R. Jaff, "Medical treatment of peripheral arterial disease: A comprehensive review," *J. Vasc. Interv. Radiol.* **15**, 1197–1207 (2004).

²G. J. Hankey, P. E. Norman, and J. W. Eikelboom, "Medical treatment of peripheral arterial disease," *JAMA, J. Am. Med. Assoc.* **295**, 547–553 (2006).

³K. Watson, B. D. Watson, and K. S. Pater, "Peripheral arterial disease: A review of disease awareness and management," *Am. J. Geriatr. Pharmacother.* **4**, 365–379 (2006).

⁴A. T. Hirsch *et al.*, "ACC/AHA guidelines for the management of patients with peripheral arterial disease (lower extremity, renal, mesenteric, and abdominal aortic): A collaborative report from the American Association for Vascular Surgery/Society for Vascular Surgery, Society for Cardiovascular Angiography and Interventions, Society for Vascular Medicine and Biology, Society of Interventional Radiology, and the ACC/AHA Task Force on Practice Guidelines (writing committee to develop guidelines for the management of patients with peripheral arterial disease)—Summary of recommendations," *J. Vasc. Interv. Radiol.* **17**, 1383–1398 (2006).

⁵A. T. Hirsch *et al.*, "ACC/AHA 2005 guidelines for the management of patients with peripheral arterial disease (lower extremity, renal, mesenteric, and abdominal aortic): Executive summary a collaborative report from the American Association for Vascular Surgery/Society for Vascular Surgery, Society for Cardiovascular Angiography and Interventions, Society for Vascular Medicine and Biology, Society of Interventional Radiology, and the ACC/AHA Task Force on Practice Guidelines (Writing Committee to Develop Guidelines for the Management of Patients With Peripheral Arterial Disease) endorsed by the American Association of Cardiovascular and Pulmonary Rehabilitation; National Heart, Lung, and Blood Institute; Society for Vascular Nursing; Transatlantic Inter-Society Consensus; and Vascular Disease Foundation," *J. Am. Coll. Cardiol.* **47**, 1239–1312 (2006).

⁶D. Chan, M. E. Anderson, and B. L. Dolmatch, "Imaging evaluation of lower extremity infrainguinal disease: Role of the noninvasive vascular laboratory, computed tomography angiography, and magnetic resonance angiography," *Tech. Vasc. Interv. Radiol.* **13**, 11–22 (2010).

⁷F. U. Grijalba and M. C. Esandi, "Comparison of gadofosveset-enhanced three-dimensional magnetic resonance angiography with digital subtraction angiography for lower-extremity peripheral arterial occlusive disease," *Acta Radiol.* **51**, 284–289 (2010).

⁸Y. Matignon, "Échographie-Doppler dans l'Artériopathie Oblitérante des Membres Inférieurs (Agence Nationale d'Accréditation et d'Évaluation en Santé, 2004), pp. 1–144.

⁹S. D. Boskovic and A. N. Neskovic, "Atherosclerosis plaque regression," *Med. Pregl.* **59**, 38–45 (2006).

¹⁰B. H. Elsmann, D. A. Legemate, H. J. de Vos, W. P. Mali, and B. C. Eikelboom, "Hyperaemic colour duplex scanning for the detection of aortoiliac stenoses. A comparative study with intra-arterial pressure measurement," *Eur. J. Vasc. Endovasc Surg.* **14**, 462–467 (1997).

¹¹J. I. Weitz, J. Byrne, G. P. Clagett, M. E. Farkouh, J. M. Porter, D. L. Sackett, D. E. Strandness, Jr., and L. M. Taylor, "Diagnosis and treatment of chronic arterial insufficiency of the lower extremities: A critical review," *Circulation* **94**, 3026–3049 (1996).

¹²L. E. Chambless, M. M. Zhong, D. Arnett, A. R. Folsom, W. A. Riley, and G. Heiss, "Variability in B-mode ultrasound measurements in the atherosclerosis risk in communities (aric) study," *Ultrasound Med. Biol.* **22**, 545–554 (1996).

¹³T. R. Nelson, "Three-dimensional imaging," *Ultrasound Med. Biol.* **26**, S35–S38 (2000).

- ¹⁴W. Birkfellner, F. Watzinger, and F. Wanschitz, "Systematic distortions in magnetic position digitizers," *Med. Phys.* **25**, 2242–2248 (1998).
- ¹⁵M. Cartellieri, F. Vorbeck, and J. Kremser, "Comparison of different 3D navigation systems by a clinical user," *Acta. Arch. Otolaryngol.* **258**, 38–41 (2001).
- ¹⁶D. D. Frantz, A. D. Wiles, S. E. Leis, and S. R. Kirsh, "Accuracy assessment protocols for electromagnetic tracking systems," *Phys. Med. Biol.* **48**, 2241–2251 (2003).
- ¹⁷L. Mercier, T. Lango, F. Lindseth, and D. L. Collins, "A review of calibration techniques for freehand 3-D ultrasound systems," *Ultrasound Med. Biol.* **31**, 449–471 (2005).
- ¹⁸F. Rousseau, "Méthodes d'analyse d'image et de calibration pour l'échographie 3D en mode main-libre," Ph.D. thesis, Institut de Formation Supérieur en Informatique et Communication, VISTA (IRISA, Rennes), 15 December 2003.
- ¹⁹G. Duchemin, P. Poignet, E. Dombre, and F. Pierrot, "Medically safe and sound," *IEEE Rob. Autom. Mag.* **11**, 46–55 (2004).
- ²⁰P. Abolmaesumi, S. E. Salcudean, W.-H. Zhu, M. R. Sirospour, and S. P. DiMaio, "Image-guided control of a robot for medical ultrasound," *IEEE Trans. Rob. Autom.* **18**, 11–23 (2002).
- ²¹P. Arbeille, G. Poisson, P. Vieyres, J. Ayoub, M. Porcher, and J. L. Boulay, "Echographic examination in isolated sites controlled from an expert center using a 2-D echograph guided by a teleoperated robotic arm," *Ultrasound Med. Biol.* **29**, 993–1000 (2003).
- ²²F. Pierrot, E. Dombre, E. Dégoulangue, L. Urbain, P. Caron, S. Boudet, J. Gariépy, and J.-L. Mégny, "Hippocrate: A safe robot arm for medical applications with force feedback," *Med. Image Anal.* **3**, 285–300 (1999).
- ²³A. Vilchis, J. Troccaz, P. Cinquin, K. Masuda, and F. Pellissier, "A new robot architecture for tele-echography," *IEEE Trans. Rob. Autom.* **19**, 922–926 (2003).
- ²⁴M. A. Janvier, L. G. Durand, M.-H. Roy Cardinal, I. Renaud, B. Chayer, P. Bigras, J. de Guise, G. Soulez, and G. Cloutier, "Performance evaluation of a medical robotic 3D-ultrasound imaging system," *Med. Image Anal.* **12**, 275–290 (2008).
- ²⁵S. Dandekar, Y. Li, J. Molloy, and J. Hossack, "A phantom with reduced complexity for spatial 3-D ultrasound calibration," *Ultrasound Med. Biol.* **31**, 1083–1093 (2005).
- ²⁶P.-W. Hsu, R. W. Prager, A. H. Gee, and G. M. Treece, "Rapid, easy and reliable calibration for freehand 3D ultrasound," *Ultrasound Med. Biol.* **32**, 823–835 (2006).
- ²⁷P. R. Detmer, G. Bashein, T. Hodges, K. W. Beach, E. P. Filer, D. H. Burns, and D. E. Strandness, Jr., "3D ultrasonic image feature localization based on magnetic scanhead tracking: In vitro calibration and validation," *Ultrasound Med. Biol.* **20**, 923–936 (1994).
- ²⁸A. Hartov, S. D. Eisner, M. S. David, W. Roberts, K. D. Paulsen, L. A. Platenik, and M. I. Miga, "Error analysis for a free-hand three-dimensional ultrasound system for neuronavigation," *Neurosurg. Focus.* **6** No. 3: article 5 (1999).
- ²⁹D. F. Leotta, P. R. Detmer, and R. W. Martin, "Performance of a miniature magnetic position sensor for three-dimensional ultrasound imaging," *Ultrasound Med. Biol.* **23**, 597–609 (1997).
- ³⁰R. W. Prager, R. N. Rohling, A. H. Gee, and L. Berman, "Rapid calibration for 3-D freehand ultrasound," *Ultrasound Med. Biol.* **24**, 855–869 (1998).
- ³¹F. Lindseth, G. A. Tangen, T. Lango, and J. Bang, "Probe calibration for freehand 3-D ultrasound," *Ultrasound Med. Biol.* **29**, 1607–1623 (2003).
- ³²N. Pagoulatos, D. R. Haynor, and Y. Kim, "A fast calibration method for 3-D tracking of ultrasound images using a spatial localizer," *Ultrasound Med. Biol.* **27**, 1219–1229 (2001).
- ³³P. W. Hsu, R. W. Prager, A. H. Gee, and G. M. Treece, "Real-time freehand 3D ultrasound calibration," *Ultrasound Med. Biol.* **34**, 239–251 (2008).
- ³⁴L. G. Bouchet, S. L. Meeks, G. Goodchild, F. J. Bova, J. M. Buatti, and W. A. Friedman, "Calibration of three-dimensional ultrasound images for image-guided radiation therapy," *Phys. Med. Biol.* **46**, 559–577 (2001).
- ³⁵J. F. Polak, *Peripheral Vascular Sonography*, 2nd ed. (Lippincott Williams & Wilkins, Philadelphia, 2004).
- ³⁶F. Lindseth, J. Bang, and T. Lango, "A robust and automatic method for evaluating accuracy in 3-D ultrasound-based navigation," *Ultrasound Med. Biol.* **29**, 1439–1452 (2003).
- ³⁷G. Cloutier, S. D. Qanadli, P. Teppaz, L. Allard, Z. Qin, F. Cloutier, and L.-G. Durand, "A multimodality vascular imaging phantom with fiducial markers visible in DSA, CTA, MRA, and ultrasound," *Med. Phys.* **31**, 1424–1433 (2004).
- ³⁸C. Bertolotti, Z. Qin, B. Lamontagne, L. G. Durand, G. Soulez, and G. Cloutier, "Influence of multiple stenoses on echo-Doppler functional diagnosis of peripheral arterial disease: A numerical and experimental study," *Ann. Biomed. Eng.* **34**, 564–574 (2006).
- ³⁹M.-H. Roy Cardinal, J. Meunier, G. Soulez, R. L. Maurice, E. Therasse, and G. Cloutier, "Intravascular ultrasound image segmentation: A three-dimensional fast-marching method based on gray level distributions," *IEEE Trans. Med. Imaging* **25**, 590–601 (2006).
- ⁴⁰D. F. Leotta, J. F. Primozich, K. W. Beach, R. O. Bergelin, and D. E. Strandness, Jr., "Serial measurement of cross-sectional area in peripheral vein grafts using three-dimensional ultrasound," *Ultrasound Med. Biol.* **27**, 61–68 (2001).
- ⁴¹K. F. Dajani, "Analysis of carotid and femoral stenosis and lesions with three-dimensional ultrasound," Ph.D. thesis, The University of Toledo, Ohio, August 2000.
- ⁴²K. M. Kanal, J. M. Kofler, and D. S. Groth, "Comparison of selected ultrasound performance tests with varying overall receiver gain and dynamic range, using conventional and magnified field of view," *Med. Phys.* **25**, 642–647 (1998).
- ⁴³F. Rousseau, P. Hellier, M. M. J. Letteboer, W. J. Niessen, and C. Barillot, "Quantitative evaluation of three calibration methods for 3-D freehand ultrasound," *IEEE Trans. Med. Imaging* **25**, 1492–1501 (2006).
- ⁴⁴A. Krupa, "Automatic calibration of a robotized 3D ultrasound imaging system by visual servoing," presented at the Proceedings of the IEEE Conference on International Robotics and Automation, Orlando, FL, 2006, pp. 4136–4141.
- ⁴⁵E. Von Lavante and J. A. Noble, "Segmentation of breast cancer masses in ultrasound using radio-frequency signal derived parameters and strain estimates," presented at the Proceedings of the IEEE International Symposium on Biomedical Imaging: From Nano to Macro, Paris, France, 2008, pp. 536–539.
- ⁴⁶X. Wen, S. E. Salcudean, and P. D. Lawrence, "Detection of brachytherapy seeds using ultrasound radio frequency signals," presented at the Proceedings of the Medical Imaging Conference 2006: Ultrasonic Imaging and Signal Processing, San Diego, CA, 2006, pp. 61470J-1–61470J-8.
- ⁴⁷C. P. Allott, C. D. Barry, R. Pickford, and J. C. Waterton, "Volumetric assessment of carotid artery bifurcation using freehand-acquired, compound 3D ultrasound," *Br. J. Radiol.* **72**, 289–292 (1999).
- ⁴⁸D. F. Leotta, J. F. Primozich, K. W. Beach, R. O. Bergelin, K. D. Gibson, and D. E. Strandness, Jr., "Cross-sectional area changes in peripheral vein grafts monitored by three-dimensional ultrasound imaging," presented at the Proceedings of the IEEE Ultrasonics Symposium, San Juan, Puerto Rico, 2000, pp. 1865–1868.
- ⁴⁹D. F. Leotta and R. W. Martin, "Three-dimensional spatial compounding of ultrasound scans with weighting by incidence angle," *Ultrasound Med. Biol.* **22**, 1–19 (2000).
- ⁵⁰C. D. Barry, C. P. Allott, N. W. John, P. M. Mellor, P. A. Arundel, D. S. Thomson, and J. C. Waterton, "Three-dimensional freehand ultrasound: Image reconstruction and volume analysis," *Ultrasound Med. Biol.* **23**, 1209–1224 (1997).
- ⁵¹D. C. Barratt, B. B. Ariff, K. N. Humphries, S. A. Thom, and A. D. Hughes, "Reconstruction and quantification of the carotid artery bifurcation from 3-D ultrasound images," *IEEE Trans. Med. Imaging* **23**, 567–583 (2004).
- ⁵²M. Lécant, M.-H. Roy Cardinal, Z. Qin, G. Soulez, and G. Cloutier, "In vitro in-stent restenoses evaluated by 3D ultrasound," *Med. Phys.* **36**, 513–522 (2009).